Numerical Design Analysis of Energy-Spread Monitor Using Multi-Stripline Electrodes

T. Suwada

***Abstract*—A new energy-spread monitor is under development in order to control the transverse positions and energy spread of a single-bunch positron beam with charges of 4 nC. This monitor is to be installed at a dispersion section of the beam transport line (E = 1.1 GeV) for the positron beam transporting from the linac to a damping ring towards the Super KEK B-factory. The author proposes the use of this new monitor consisting of multi-stripline electrodes in order to simultaneously measure not only the transverse beam positions but also the energy spread pulse-by-pulse. This report describes in detail the basic design of the energy-spread monitor, its detection sensitivity and its characteristics depending on the transverse positions and energy spread of the positron beam based on numerical simulations.**

I. Introduction

The Super KEK B-factory project (SKEKB) [1] is a next-generation B-factory that has been under construction at KEK after the KEK B-factory project [2] was discontinued in 2010. The SKEKB is an electron–positron collider with asymmetric energies, and it comprises 4-GeV positron (LER) and 7-GeV electron (HER) rings. The target luminosity of the SKEKB is 40 times the peak luminosity of the KEKB. The SKEKB is being commissioned based on the urgent need to perform high-energy flavor particle physics experiments concerning the CP violation in B mesons [3].

The KEKB linac [4] is the injector linac for the SKEKB rings. The injector linac is also being concurrently upgraded for the above-mentioned purpose [5]–[7]. The requirements of the injector linac are to deliver low-emittance and high-current electron and positron beams to the SKEKB rings. A low-emittance and high-current electron beam is to be generated by using a new photo-cathode RF gun [8], [9]. On the other hand, the low-emittance and high-current positron beam is to be generated by bombarding a tungsten target with high-energy primary electrons with an energy of 3.5 GeV and electron charges of 10 nC. The positrons are to be efficiently captured using a new flux concentrator and large aperture S-band accelerating structures [10], which are to be damped to the level required for the low-emittance beam through a new damping ring (DR) [11].

The new DR with a circumference length of 136 m is under construction alongside the end section of sector 2 in the linac, and it is to be connected to the linac-to-DR transport line (LTR) at the second beam switchyard (SY2) where the beam energy is 1.1 GeV. Under actual operation, since the energy spread of the positron beam is very large in comparison with the acceptance of the DR ($\pm 1.5\%$), particularly in its low energy tail, the energy tail is planned to be cut with a series of collimators, and the energy spread is to be compressed up to $\pm 1.5\%$ from $\pm 5\%$ by an energy compression system (ECS) comprising 41-MV S-band accelerating structures that are to be installed in the LTR [11]. The positron beams shall be extracted after 40 ms from the DR. After the positron beams are delivered from the DR, the bunch length of the positron beam is to be reduced by an order of magnitude with a bunch compression system (BCS) installed at the DR-to-linac transport line (RTL) in order to ensure that the energy spread is reduced to as small a value as possible, which is generated with the RF curvature of the downstream linac accelerating sections. The positron beams shall subsequently be transported back through the RTL to the SY2, and again accelerated up to 4.0 GeV in the linac for injection into the SKEKB LER.

The specifications of the electron and positron injection beams are summarized in Table I. Here, for purposes of comparison, the electron and positron beam specifications for the previous KEKB are also listed.

TABLE I
Beam specifications for the injector linac

	KEKB (e^-/e^+)	SKEKB (e^-/e^+)
Injection energy E [GeV]	8.0 / 3.5	7.0 / 4.0
Bunch charge Q [nC]	1.0 / 1.0 (10*)	5.0 / 4.0 (10*)
Number of bunches / pulse	2 / 2	2 / 2
Emittance $\gamma\epsilon$ [μm]	300 / 2100	20 / $92_{[H]}$: $7_{[V]}$
Energy spread δ [%]	0.05 / 0.125	0.08 / 0.07**
Bunch length l [mm]	1.3 / 2.6	1.3 / 0.7#
(*) for primary electrons	(**) with ECS	(#) with BCS

Because the SKEKB is a B-factory machine, precise operation of the injector linac is required for minimizing the tuning time and maximizing its stability in operation. Although stable control of the beam positions and energies at several sectors throughout the beam-position and energy-feedback systems are essential even to the SKEKB operation, the energy spreads of the injection beams are often enlarged due to the long-term phase drift induced by high-power and booster klystrons. Thus, beam diagnostic and monitoring tools are required to tune the beam-energy spreads; furthermore these tools are also expected to control the longitudinal wakefields that are mainly generated at the accelerating structures, particularly at the LTR in SY2.

The energy-spread monitor (ESM) is a very useful monitoring tool to cater to such requirements. The ESM detects

T. Suwada is with Accelerator Laboratory, High Energy Accelerator Research Organization (KEK) and the Graduate University for Advanced Studies School of High Energy Accelerator Science, 1-1 Oho, Tsukuba, Ibaraki, 305-0801 Japan and (e-mail: tsuyoshi.suwada@kek.jp).

both the transverse beam positions and the energy spread at large dispersion sections by measuring any variations in the electromagnetic field distribution induced in the multi-stripline electrodes located in the monitor.

The ESM has been newly designed by numerical simulations based on the electrostatic analysis of a charged beam. It is expected that with such ESMs, the energy spread could be made as small as possible under real-time operation within a resolution of the order of 10^{-4} along with transverse position control of the order of less than 0.1 mm with the use of suitable detection electronics.

II. Energy-spread monitor

A. Specifications of positron beam at SY2

The positrons are captured with a flux concentrator and accelerated up to an energy of 120 MeV using large-aperture S-band accelerating structures. The subsequently positioned normal S-band accelerating structures accelerate the positrons up to an energy of 1.1 GeV at SY2 and the positron beam is injected into the DR through the LTR. The specifications of the positron beam and the optics parameters at SY2 are summarized in Table II [11].

TABLE II
Specifications and optics parameters for the positron beam at SY2

	Horizontal	Vertical
β [m]	6.26	6.08
Dispersion η [m]	0.639	0
R_{56} [m]	-0.64	-1.0
Emittance ϵ [μm]	0.5	0.5
Beam size σ [mm]	3.8*	1.7
Energy E [GeV]	1.1	
Energy spread δ [%]	2.3	
Bunch length l [mm]	5.0#	

(*) average rms width (#) fwhm

B. Basic design

A new multi-stripline-type ESM is under development in order to measure the energy spread and beam positions of the positron beam at a location of the quadrupole magnet (QLF1N) installed immediately after the first bending magnet of the LTR at SY2. The ESM is to be installed inside this quadrupole magnet.

The ESM comprises eight stripline electrodes attached to the inner surface of a racetrack chamber along the beam axis as shown in Fig. 1. The lengths of the inner major and minor axes in the cross section of the chamber are 120 mm and 44 mm, respectively. Each electrode comprises a 50-Ω parallel stripline with a longitudinal length of 132.5 mm, width of 10 mm, and thickness of 1.5 mm. An SMA vacuum feedthrough is connected to the upstream side of each electrode, while the downstream end is short-circuited to the chamber ground.

Although the electrodes are arranged at regular distances of 20 mm along the horizontal direction, the electrodes located on the upper and lower surfaces are asymmetrically configured. This means that the four electrodes on the upper surface are shifted from the center position by -5 mm while those on the lower surface are shifted from the center position by 5 mm. By implementing such a nesting structure for the electrode configuration, the transverse spatial spread of the beam can be more precisely measured in comparison with the conventionally used symmetric electrode configuration. The electrode width is selected mainly from the viewpoint of the signal-to-noise ratio. The cross-sectional area of the chamber is chosen such that the positron beam can be completely pass through even with a relatively large energy spread within the aperture of the chamber.

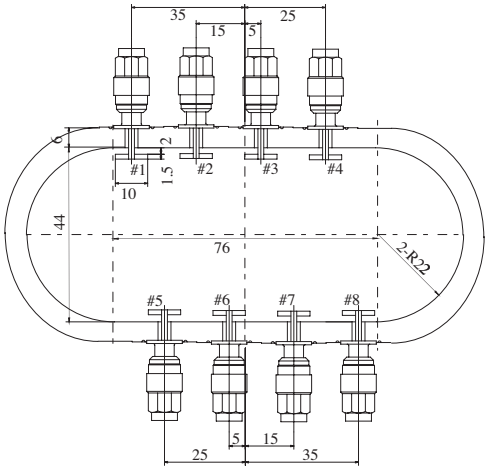

Fig. 1. Cross-sectional view of the energy-spread monitor. The lengths are specified in units of mm.

III. Simulation method

Numerical analysis for the ESM design was carried out by means of the charge-simulation method [12], [13]. Here, only a brief overview of this method is provided to discuss the ESM analysis in the following section.

The electromagnetic field generated by a relativistic charged beam inside a vacuum chamber is greatly boosted in the transverse direction in terms of the beam axis due to Lorentz contraction. This phenomenon implies that the electromagnetic coupling of the electrodes to the beam can be treated as a two-dimensional electrostatic potential problem when the bunch structure of the beam in the longitudinal direction is not taken into account. Thus, the electromagnetic analysis of the ESM can be simply considered as an electrostatic potential problem only in the transverse plane.

The charge-simulation method is based on one of the boundary element methods used for analyzing such electrostatic potential problems. In this method, at certain boundary points, imaginary and real charges are introduced in order to analyze a given electrostatic field system. The boundary points are arranged on all the boundary surfaces of the conductors in the system. An imaginary charge is placed in the immediate vicinity of each boundary point in a one-to-one manner (see Fig. 2).

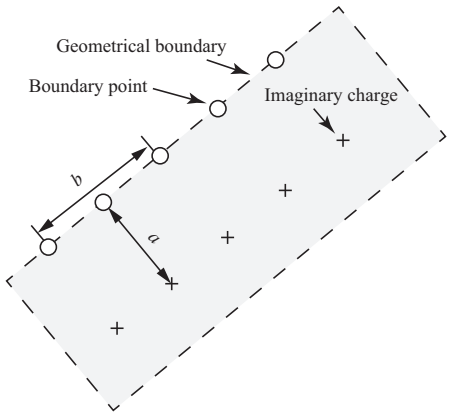

Fig. 2. Arrangement of boundary points on a conductor surface and their corresponding imaginary charges.

If the length between a given boundary point and the corresponding imaginary charge is a and the length between alternating neighboring boundary points is b, we have the following relation

$$a = b \times f, \tag{1}$$

where f denotes a free parameter that is used to determine the minimal spatial sizes for calculating the electrostatic fields in the system. The parameter f requires to be determined by numerical calculations for the electrostatic equipotential line to stably reproduce the boundary of the conductor within allowable calculation errors (generally chosen in the range of 0.2–1.5). The electrostatic potentials at the boundary points of each conductor and also at any spatial points can be calculated so as to satisfy the boundary conditions of the system by using the linear superposition principle of electrostatic fields contributed by all the imaginary charges. If there are real charges in the system, they also contribute via linear superposition to generate electrostatic fields along with the imaginary charges.

IV. Application to ESM

A. Segmentation of boundary surfaces

All the boundary surfaces of the chamber and electrodes are segmented as shown in Fig. 2. The boundary points on the inner surface of the chamber are arranged as n points spaced at equal intervals. The outer surface of each electrode is segmented by $l \times m$ points along the horizontal (x) and vertical (y) directions, respectively. The segmentation numbers (l, m, n) are decided based on the convergency study of the electrostatic-field analysis. The electrostatic fields satisfying all the boundary conditions in a given system are uniquely found by the uniqueness theorem in electrostatic boundary-value problems.

The rectangular coordinates (x_i,y_i) of the boundary points on the inner surface of the chamber in both the upper and lower straight sections are given as:

$$x_i = w\left(\frac{1}{2} - \frac{i}{n}\right) \ (1 \le i \le n), \tag{2}$$

$$y_i = \pm\frac{h}{2}, \tag{3}$$

where $w = 76$ mm and $h = 44$ mm indicate the width of the inner surface and the height between the top and bottom sections of the inner surfaces, respectively. The coordinates (X_j,Y_j) of the imaginary charges are given as:

$$X_j = w\left(\frac{1}{2} - \frac{j}{n}\right) \ (1 \le j \le n), \tag{4}$$

$$Y_j = \pm\frac{h}{2} \pm a, \tag{5}$$

where the sign ($\pm$) is selected by the double sign correspondence so that the imaginary charges are adequately located just along the positive and negative directions for the upper ($+$) and lower ($-$) surface boundaries, respectively. For the arc section of the chamber, the segmentation length between the neighboring boundary points is set to be the same as that defined for the straight surface boundary.

For the electrodes, a similar segmentation method is applied as follows:

$$x_i = w_e\left(\frac{1}{2} - \frac{i}{l}\right) \ (1 \le i \le l), \tag{6}$$

$$y_i = t_e\left(\frac{1}{2} - \frac{i}{m}\right) \ (1 \le i \le m), \tag{7}$$

where $w_e = 10$ mm and $t_e = 1.5$ mm indicate the width and thickness of the electrode, respectively. The coordinates (X_j, Y_j) of the imaginary charges are similarly given as:

$$X_j = w_e\left(\frac{1}{2} - \frac{j}{l}\right) \ (1 \le j \le l), \tag{8}$$

$$Y_j = t_e\left(\frac{1}{2} - \frac{j}{m} \pm \frac{a}{t_e}\right) \ (1 \le j \le m), \tag{9}$$

where the sign ($\pm$) is again selected by the double sign correspondence so that the imaginary charges are properly located just inside the surface boundary.

B. Segmentation of asymmetrically spread beam

The transverse spatial distribution of the beam charges at SY2 is complicated; however, here, for simplicity, the transverse charge distribution (Q_b) inside the chamber is assumed to be expressed by asymmetric and symmetric Gaussian functions along the x and y directions, respectively. The transverse charge distribution is assumed to be given by

$$\begin{aligned} Q_b(x,y) = Q_0 \ \exp\left[-\frac{(y-y_0)^2}{2\sigma_y^2}\right] \\ \times \left\{[1-\theta(x-x_0)]\exp\left[-\frac{(x-x_0)^2}{2\sigma_L^2}\right]\right. \\ \left. + \ \theta(x-x_0)\exp\left[-\frac{(x-x_0)^2}{2\sigma_H^2}\right]\right\}, \end{aligned} \tag{10}$$

where (x_0, y_0) denotes the peak coordinate position of the asymmetric charge distribution, Q_0 denotes the peak charge at $x = x_0$ and $y = y_0$, σ_L (σ_H) denotes the one-sigma horizontal charge width in the region of $x < x_0$ ($x > x_0$) in the asymmetric Gaussian distribution, and σ_y denotes the

one-sigma vertical charge width in the symmetric Gaussian distribution. Here, $\theta(u)$ denotes a step function defined as

$$\theta(u) = \begin{cases} 0 & (u < 0), \\ 1 & (u > 0). \end{cases} \quad (11)$$

The parameters of average rms charge width (σ) and asymmetry (A) are defined as

$$\sigma = \frac{\sigma_L + \sigma_H}{2}, \quad (12)$$

$$A = \frac{\sigma_L - \sigma_H}{\sigma_L + \sigma_H}, \quad (13)$$

for which the converse relations $\sigma_L = \sigma(1 + A)$ and $\sigma_H = \sigma(1 - A)$ are also satisfied. The asymmetric real charges are segmented by similar segmentation numbers applied to the electrodes within a region of three-sigma in the asymmetric Gaussian distribution function.

C. Electrostatic field analysis

The electrostatic potential (V_i^k) on the i-th boundary point of the k-th electrode surface (for simplicity, k = 0 is assigned to the chamber surface) can be calculated by linearly superposing the potentials (V_{ij}^k and V_{im}^b) contributed by all the imaginary (q_j^k) and real (q_m^b) charges, respectively, as follows:

$$V_i^k = \sum_j V_{ij}^k + \sum_m V_{im}^b, \quad (14)$$

$$= \sum_j P_{ij} q_j^k + \sum_m P_{im} q_m^b, \quad (15)$$

$$P_{ij} = -\frac{1}{2\pi\epsilon_0} \ln r_{ij} + C, \quad (16)$$

$$r_{ij} = \sqrt{(X_j - x_i)^2 + (Y_j - y_i)^2}, \quad (17)$$

where P_{ij} and r_{ij} denotes the potential coefficient upon assuming a line charge of infinite length and the length between the i-th boundary point and the j-th imaginary (or real) charge, respectively, ϵ_0 denotes the dielectric constant in vacuum, and C denotes the integration constant.

The boundary conditions in this analysis are given as follows:

1 The electrostatic potential (V_i^0) on the inner surface of the chamber is equal to zero (ground potential),

$$V_i^0 = 0; \quad (18)$$

2 The electrostatic potential ($V_i^k (k \neq 0)$) on the surface of the k-th electrode is equal to zero (short-circuited),

$$V_i^k = 0; \quad (19)$$

3 The summation of all the imaginary charges induced on the chamber surface (Q_c) and on all the electrodes (Q_e), and all the real charges (Q_b) by the beam is conserved to be zero as per the charge conservation law,

$$Q_c + Q_e + Q_b = 0. \quad (20)$$

Here, the summation relations for the segmented charges are defined as

$$Q_c = \sum_j q_j^0 \ (k = 0), \quad (21)$$

$$Q_e = \sum_k Q_e^k, \ Q_e^k = \sum_j q_j^k \ (k \neq 0), \quad (22)$$

$$Q_b = \sum_m q_m^b, \quad (23)$$

where Q_e^k $(k \neq 0)$ denotes the summation of all the imaginary charges (q_j^k) on the k-th electrode. Based on these three boundary conditions, the imaginary charges on each electrode can be calculated by solving the simultaneous linear equations (eq. (15)) obeying the boundary conditions (eqs. (18)-(20)).

The imaginary charge (Q_e^k) induced on the k-th electrode is proportional to the pick-up voltage of the electrode. Thus, the electrostatic characteristics and sensitivity of the ESM depending on the spacial charge width and transverse positions of the beam can be numerically simulated based on electrostatic analysis within allowable calculation errors.

V. Simulation results

A. Convergency study

In order to ensure accurate simulation results, we performed a convergency study by positioning a point charge at the center position of the ESM by changing the segmentation numbers (l, m, n) for the boundary points and imaginary charges induced on the chamber and electrode surfaces.

The segmentation numbers were simulated based on a series of refined computational boundary points until a steady state of the induced charges was obtained. The typical results are shown in Fig. 3. Fig. 3 (a) shows the variation in the summation of all the imaginary charges (Q_c) induced on the chamber surface and Fig. 3 (b) shows the summation of the imaginary charges (Q_e) induced on all the electrode surfaces as a function of b and the segmentation parameter f.

The convergency values are obtained to be approximately 0.4% and 1.4% for Q_e and Q_c at $b = 0.5$ mm, respectively, at segmentation numbers $(l, m, n) = (6, 20, 76)$. These convergence values are sufficiently small to obtain sufficient resolution for simulating the imaginary charges induced on the electrodes within a level of 0.4% upon taking into account the allowable computation time in simulation calculations.

The total number of segmentation parameters including the segmentation of the spread beam charges has been fixed to be 675 in order to be efficiently solved to obtain precise values of the electrostatic physical parameters in the ESM analysis.

B. Beam-position analysis for asymmetrically spread beam

Based on the beam dynamics in accelerator physics [14], the horizontal beam size (σ_x) at a section with a horizontal dispersion of η_x is represented as

$$\sigma_x = \sqrt{\beta_x \epsilon_x + (\eta_x \delta)^2}, \quad (24)$$

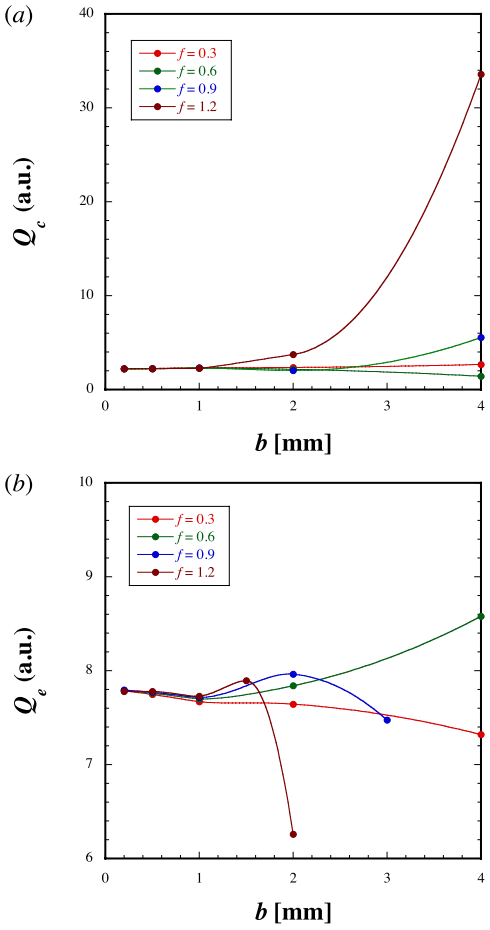

Fig. 3. Variations in convergence on the imaginary charge summations, (a) Q_c and (b) Q_e as functions of b and the segmentation parameter f.

where β_x, ϵ_x and δ denote the horizontal β-function, geometrical emittance, and energy spread at the dispersion section, respectively. The vertical beam size is also similarly described. It can be deduced that the beam size increases depending on the energy spread along with increase in the emittance while the intrinsic beam size is determined by the emittance value that depends on the beam optics at the dispersion section. Since the dispersion functions are η_x = 0.639 m and η_y = 0 m along the horizontal and vertical directions at the location of the QLF1N, respectively, the vertical beam size is determined only by the intrinsic emittance value. The transverse positions of the beam with a given energy spread can be obtained by analyzing the electrostatic field distribution generated by spatially spread charges in the transverse plane at the ESM.

Here, it is useful to introduce algebraic parameters related to the signal intensities of the electrodes. These parameters are defined as

$$Q_e^{x+} \equiv \sum_{k=3}^{4} Q_e^k + \sum_{k=7}^{8} Q_e^k, \quad (25)$$

$$Q_e^{x-} \equiv \sum_{k=1}^{2} Q_e^k + \sum_{k=5}^{6} Q_e^k, \quad (26)$$

$$Q_e^{y+} \equiv \sum_{k=1}^{4} Q_e^k, \quad (27)$$

$$Q_e^{y-} \equiv \sum_{k=5}^{8} Q_e^k, \quad (28)$$

$$\Sigma \equiv \sum_{k=1}^{8} Q_e^k, \quad (29)$$

$$\Delta_x \equiv Q_e^{x+} - Q_e^{x-}, \quad (30)$$

$$\Delta_y \equiv Q_e^{y+} - Q_e^{y-}, \quad (31)$$

for which the allocation of the electrode number is defined as shown in Fig. 1. The beam positions are related to the parameters Δ_x/Σ, and Δ_y/Σ and the energy spread δ. The horizontal (vertical) sensitivity for the beam position, S_x (S_y), is defined at the center position by differentiating Δ_x/Σ (Δ_y/Σ) with respect to x (y) as a function of δ as follows:

$$S_x(\delta) = \frac{d}{dx}\left(\frac{\Delta_x}{\Sigma}\right). \quad (32)$$

The vertical sensitivity is defined by a similar formula. It should be noted that the position sensitivities of the ESM strongly depend on the energy spread.

The results based on a two-dimensional Δ/Σ analysis are shown in Fig. 4. Figs. 4 (a) and (b) show the variations in

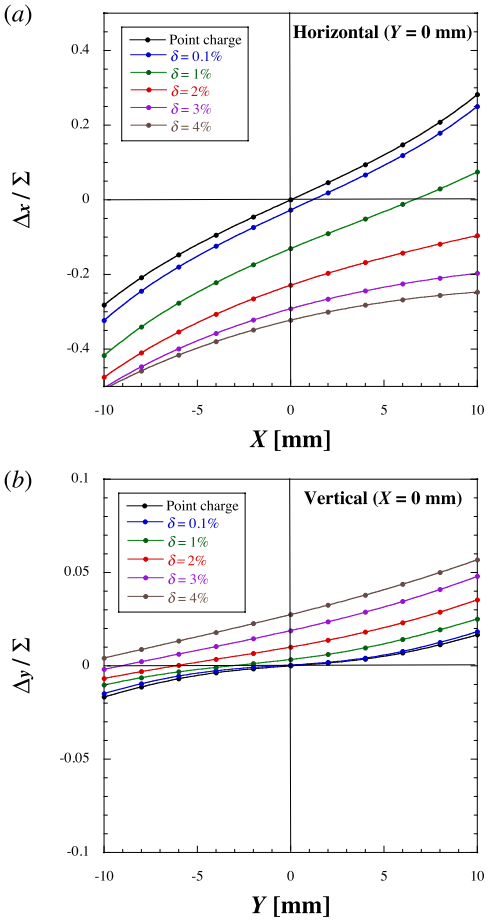

Fig. 4. Variations in (a) Δ_x/Σ and (b) Δ_y/Σ depending on x (y = 0), and y (x = 0) and δ.

Δ_x/Σ and Δ_y/Σ as functions of x (y = 0) and y (x = 0), respectively, and δ. Since the nominal energy spread of the positron beam is δ = 2.3% at SY2, the horizontal (vertical) sensitivity is calculated to be S_x = 1.58 $\times$ 10^{-2}/mm (S_y = 1.97 $\times$ 10^{-3}/mm) at the center position. The result indicates that the horizontal sensitivity is greater than the vertical one by an order. This arises due to the difference in the electrostatic field distributions generated in the racetrack-type ESM along the horizontal and vertical axes. It can be also seen that when the charge distribution of the beam is asymmetric with an energy spread, $\Delta_x/\Sigma \neq 0$ at x = 0 and $\Delta_y/\Sigma \neq 0$ at y = 0 while only for a symmetric charge distribution (or point charge) Δ_x/Σ = 0 and Δ_y/Σ = 0 at the center position are satisfied. This is because the ESM can measure the intensity centroid of the spatial charge distribution, and the offsets in the Δ/Σ curve result from the asymmetrically spread charges depending on the energy spread. The results suggest that offset calibrations should be carefully performed not only in the ESM but also in the detection electronics with test pulses. Thus, it should be noted that the beam positions can be calculated on the basis of both the Δ/Σ analysis and energy-spread analysis.

If the energy spread is known, the beam positions can be generally analyzed on the basis of a three-dimensional Δ/Σ analysis by using polynomial functions as follows:

$$x = \sum_{i=0}^{k}\sum_{j=0}^{k} a_{ij}\left(\frac{\Delta_x}{\Sigma}\right)^i\left(\frac{\Delta_y}{\Sigma}\right)^j, \quad (33)$$

$$y = \sum_{i=0}^{k}\sum_{j=0}^{k} b_{ij}\left(\frac{\Delta_x}{\Sigma}\right)^i\left(\frac{\Delta_y}{\Sigma}\right)^j, \quad (34)$$

where a_{ij} and b_{ij} denote the calibration coefficients that can be obtained by a beam-based measurement. These formulas yield calibration curves with a higher-order polynomial (generally $k \geq 3$) in the beam position measurement. A typical result for the horizontal position based on a three-dimensional Δ/Σ analysis with δ = 2.3% is shown in Fig. 5. The vertical position

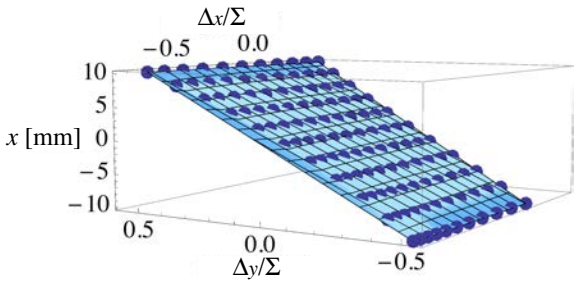

Fig. 5. Variations in the horizontal position depending on Δ_x/Σ and Δ_y/Σ (δ = 2.3%). The solid points indicate calculated data points.

can be similarly analyzed.

C. Energy-spread analysis for asymmetrically spread beam

The energy spread can be analyzed by measuring the horizontal spatial spread of the induced charge distribution because the energy spread is related to the spatial spread, as seen from eq. (24). Fig. 6 shows a typical example of the horizontal spatial spread of the induced charges for a positron beam with a nominal energy spread of δ = 2.3% at y = 0. The curve is a fitting of the calculated data of the charge distribution induced on the eight electrodes assuming that the charge distribution is along the horizontal direction with an asymmetric Gaussian function as described by eq. (10) while the vertical spatial spread is fitted with a Gaussian function. It

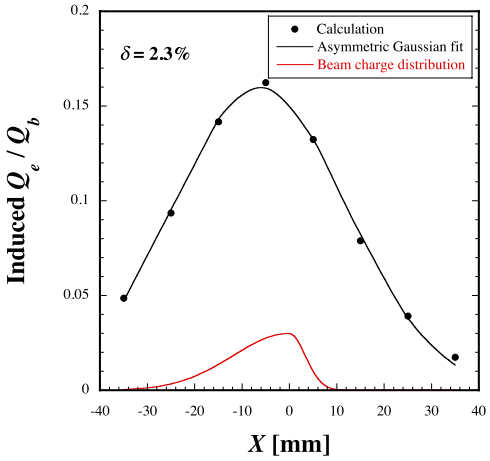

Fig. 6. Horizontal imaginary charge distribution induced on the electrodes along with the beam charge distribution with δ = 2.3% at y = 0. The solid line (black) denotes the fitting curve of the horizontal induced charge distribution with an asymmetric Gaussian function. The solid curve (red) indicates the spatial charge distribution of the beam with an asymmetric Gaussian function along the horizontal direction.

can be clearly seen that the peak position of the fitting curve is shifted along the negative direction in the horizontal axis due to the asymmetric structure of the induced charge distribution while the peak position of the beam charge distribution is set to the center position.

Fig. 7 shows the variations in the peak position (X_C) of the fitting curve as a function of the energy spread where an asymmetric Gaussian function for the horizontal beam charge distribution with a fixed asymmetry (A = 0.56) is assumed, and the peak position of the charge distribution is fixed to the center position. The dependence of the curve in terms of the energy spread becomes nonlinear with increase in the energy spread. This is because the electrostatic fields induced by the beam charges exist considerably outside the region of the electrodes in the negative direction of the horizontal axis. The differential of the fitted peak position with respect to δ at δ = 2.3% is

$$\frac{dX_C}{d\delta} = -2.7 \text{ mm}/\%. \quad (35)$$

Fig. 8 shows the variations in the width of the fitting curve on the induced charge distribution depending on the energy spread. It can be deduced that the curve becomes nonlinear with decrease in the energy spread. This is because the width varies approximately linearly in the larger energy spread region where the spatial charge spread is dominant over the energy spread in comparison with the intrinsic charge spread. At δ = 2.3%, the differential of the width with respect

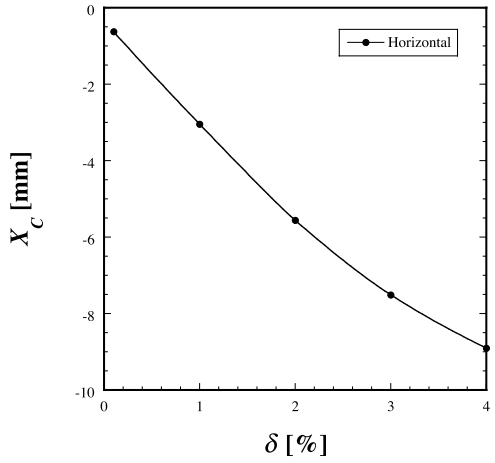

Fig. 7. Variations in the peak position of the fitting curve on the induced charge distribution depending on the energy spread. The solid line is a guide to the eye only.

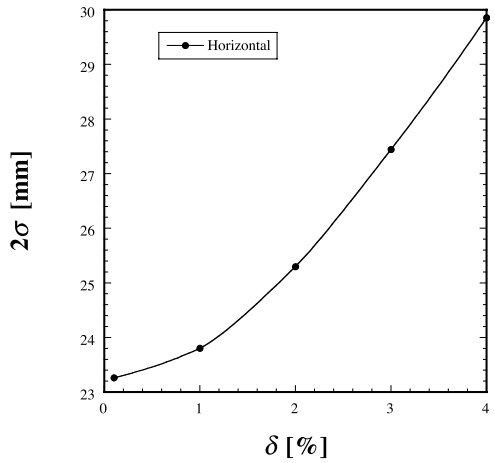

Fig. 8. Variations in the width of the fitting curve on the induced charge distribution depending on the energy spread. The solid line is a guide to the eye only.

to δ is

$$\frac{d(2\sigma)}{d\delta} = 2.5 \text{ mm}/\%. \quad (36)$$

Figs. 9 (a) and (b) show the variations in (a) the horizontal position sensitivity and (b) Δ_x/Σ depending on the energy spread. Both S_x and Δ_x/Σ monotonically reduce with increase in the energy spread. At δ = 2.3%, S_x and Δ_x/Σ are calculated to be

$$S_x(\delta) = 0.016/\text{mm}, \quad (37)$$
$$\Delta_x/\Sigma(\delta) = -0.25. \quad (38)$$

These values also yield the corresponding calibration coefficients to estimate the energy spread.

D. Expected resolution for position and energy-spread measurements

The position resolution (σ_x) of the ESM can be approximately obtained by modifying eq. (32) as

$$\sigma_x \approx dx = S_x^{-1} d\left(\frac{\Delta_x}{\Sigma}\right), \quad (39)$$

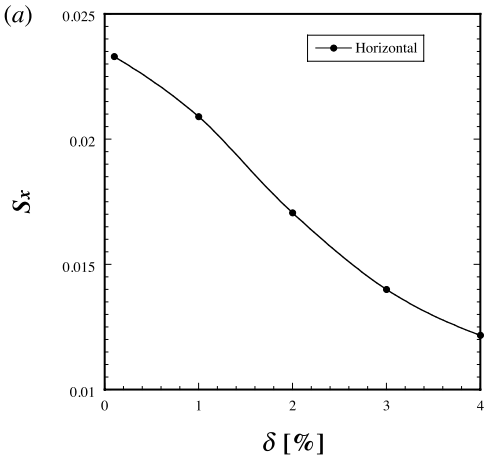

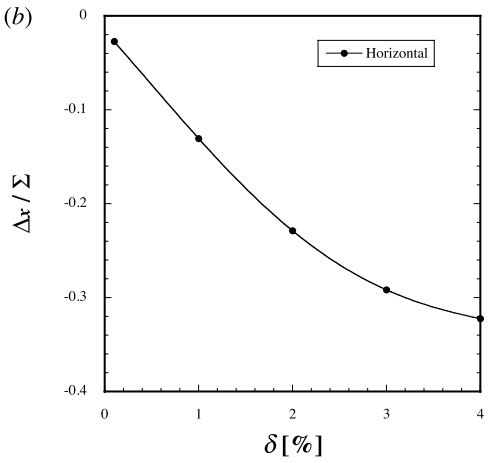

Fig. 9. Variations in (a) S_x and (b) Δ_x/Σ depending on the energy spread. Both the solid lines indicate fitting curves with a fourth-order polynomial function.

where $d(\Delta_x/\Sigma)$ is related to the resolution of the detection electronics. This parameter can be estimated by the number of bits (n_b or n_{10} in the decimal system) of an analog-to-digital circuit (ADC) embedded in the detection electronics. Here, for simplicity, assuming that the dynamic range of the detection electronics is set to the induced charge intensity at maximum (Q_m) at a certain channel, the detection resolution can be determined as $1/n_{10}$. Furthermore, it is assumed that the detection resolution is identical for all the detection channels without taking into account any noise. Thus, based on standard error analysis, the detection resolution of Δ_x/Σ can be described as

$$d\left(\frac{\Delta_x}{\Sigma}\right) \approx \frac{\sqrt{\sum_{k=1}^{8}(dQ_e^k/Q_m)^2}}{\sum_{k=1}^{8} Q_e^k/Q_m}, \approx \frac{\sqrt{8}}{n_{10}\sum_{k=1}^{8} Q_e^k/Q_m}. \quad (40)$$

The position resolution can be calculated by combining eqs. (39) and (40) as a function of the energy spread.

The resolution of the energy spread (σ_δ) can be approximately written as

$$\sigma_\delta \approx d\delta = d\left(\frac{\Delta_x}{\Sigma}\right)\left(\frac{dg(\delta)}{d\delta}\right)^{-1}, \quad (41)$$

where $g(\delta)$ denotes the fitting function in the Δ_x/Σ curve with a fourth-order polynomial, as shown in Fig. 9 (b). The resolution of the energy spread can be calculated by combining eqs. (40) and (41) as functions of the energy spread.

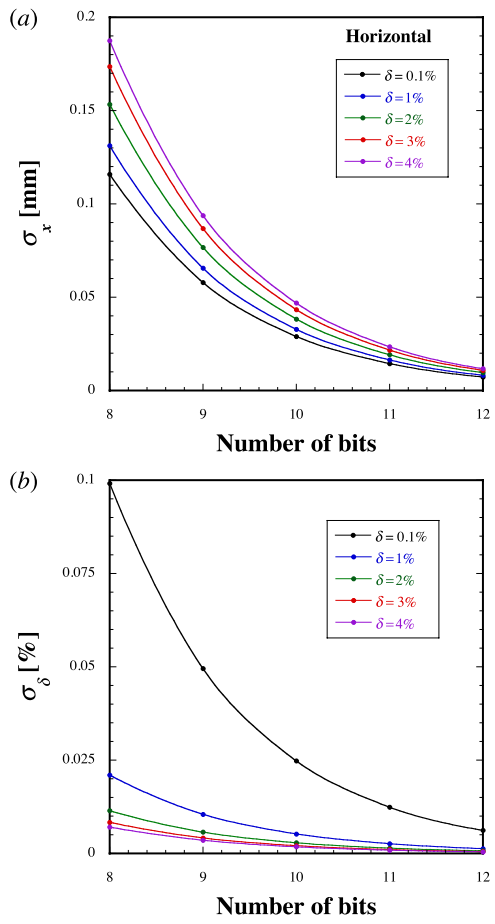

Fig. 10. Variations in the expected resolutions of (a) the position and (b) the energy spread as functions of the energy-spread value and the number of bits. The solid line is a guide to the eye only.

Figs. 10 (a) and (b) show the variations in the horizontal position and energy-spread resolution as functions of the energy-spread value and the number of bits, respectively. The typical results show that the resolutions of the position and energy spread are expected to be $\sigma_x \simeq 80$ μm and $\sigma_\delta \simeq 2 \times 10^{-4}$ at a nominal energy spread of $\delta = 2.3\%$ for an ADC with a nine-bit resolution embedded in the detection electronics. It should be noted that the transverse spatial distribution of the beam charges at SY2 is complicated; however, similar analyses can be applicable without assuming any asymmetric and symmetric Gaussian functions for the beam charge distribution in the transverse direction because all the physical parameters discussed here can be described by using measurable values.

VI. Conclusions

The basic design and systematic investigations of the detection sensitivity and characteristics of a new energy-spread monitor, which can simultaneously measure both the transverse positions and energy spread of the positron beam at SY2, have been successfully carried out by numerical simulations based on electrostatic-field analysis. The results show that detection resolutions of $\sigma_x \simeq 80$ μm (traverse position) and $\sigma_\delta \simeq 2 \times 10^{-4}$ (energy spread) can be attained at the nominal energy spread with a nine-bit ADC embedded in the detection electronics. The new ESM can be used as a beam monitoring tool in the pulse-by-pulse beam-position and energy-spread measurements at large dispersion sections.

References

[1] Y. Ohnishi, *et al.*. Theor. Exp. Phys. (2013) 03A011.
[2] T. Abe, *et al.*, Prog. Theor. Exp. Phys. (2013) 03A001.
[3] T. Abe, *et al.*, KEK Report 2010-1, edited by Z. Doležal and S. Uno.
[4] M. Akemoto, *et al.*, Prog. Theor. Exp. Phys. (2013) 03A002.
[5] T. Kamitani, M.Akemoto, D. Arakawa, M. Ikeda, A. Enomoto, S. Ohsawa,Y. Ogawa, K. Kakihara, H. Katagiri, E. Kadokura, M. Kurashina, M. Satoh, T. Shidara, A. Shirakawa, T. Sugimura, T. Suwada, T. Takenaka, K. Nakao, H. Nakajima, T. Higo, S. Fukuda, K. Furukawa, H. Honma, H. Matsushita, T. Miura, K. Mikawa, S. Matsumoto, T. Matsumoto, S. Michizono, Y. Yano, K. Yokoyama, M. Yoshida, N. Iida, M. Kikuchi, M. Tawada, T. Mimashi, Y. Kojima, K. Nakanishi, K. Hosoyama, T. Sanami, Proceedings of the XXVth International Linac Conference (LINAC10), Tsukuba, Japan, 2010, pp. 70-72.
[6] T. Higo, M. Akemoto, D. Arakawa, Y. Arakida, A. Enomoto, S. Fukuda, K. Furukawa, Y. Higashi, H. Honma, N. Iida, M. Ikeda, E. Kadokura, K. Kakihara, T. Kamitani, H. Katagiri, M. Kurashina, H. Matsushita, S. Matsumoto, T. Matsumoto, S. Michizono, K. Mikawa, T. Miura, F. Miyahara, T. Mori, H. Nakajima, K. Nakao, T. Natsui, S. Ohsawa, Y. Ogawa, M. Satoh, T. Shidara, A. Shirakawa, T. Suwada, H. Sugimoto, T. Takatomi, T. Takenaka, Y. Yano, K. Yokoyama, M. Yoshida, L. Zang, and X. Zhou (KEK, Tsukuba), D. Satoh (TIT, Tokyo), Proceedings of the 3rd International Particle Accelerator Conference (IPAC12), New Orleans, U.S.A., 2012, pp.1819-1821.
[7] K. Furukawa, M. Akemoto, D. Arakawa, Y. Arakida, A. Enomoto, S. Fukuda, H. Honma, R. Ichimiya, N. Iida, M. Ikeda, E. Kadokura, K. Kakihara, T. Kamitani, H. Katagiri, M. Kurashina, S. Matsumoto, T. Matsumoto, H. Matsushita, S. Michizono, K. Mikawa, T. Miura, F. Miyahara, T. Mori, H. Nakajima, K. Nakao, T. Natsui, Y. Ogawa, S. Ohsawa, F. Qiu, M. Satoh, T. Shidara, A. Shirakawa, H. Sugimoto, T. Suwada, T. Takatomi, T. Takenaka, M. Tanaka, Y. Yano, K. Yokoyama, M. Yoshida, L. Zang, X. Zhou (KEK, Tsukuba), D. Satoh (TIT, Tokyo), Proceedings of the 3rd International Particle Accelerator Conference (IPAC13), Shanghai, China, 2013, pp. 1583-1585.
[8] T. Natsui, M. Yoshida, X. Zhou, and Y. Ogawa, Proceedings of the 3rd International Particle Accelerator Conference (IPAC13), Shanghai, China, 2013, pp. 1117-1119.
[9] X.Zhou, T. Natsui, M. Yoshida, and Y. Ogawa, Proceedings of the 3rd International Particle Accelerator Conference (IPAC13), Shanghai, China, 2013, pp. 2965-2967.
[10] T. Kamitani, M. Akemoto, Y. Arakida, D. Arakawa, A. Enomoto, S. Fukuda, K. Furukawa, Y. Higashi, T. Higo, H. Honma, N. Iida, M. Ikeda, E. Kadokura, K. Kakihara, H. Katagiri, M. Kurashina, H. Matsushita, S. Matsumoto, T. Matsumoto, S. Michizono, K. Mikawa, T. Miura, F. Miyahara, T. Mori, H. Nakajima, K. Nakao, T. Natsui, S. Ohsawa, Y. Ogawa, M. Satoh, T. Shidara, A. Shirakawa, T. Suwada, H. Sugimoto, T. Takatomi, T. Takenaka, Y. Yano, K. Yokoyama, M. Yoshida, L. Zang, X. Zhou (KEK, Tsukuba), D. Satoh (TIT, Tokyo), Proceedings of the XXVIth International Linac Conference (LINAC12), Tel-Aviv, Israel, 2012, pp. 177-179.
[11] N. Iida, H. Ikeda, T. Kamitani, M. Kikuchi, and K. Oide, and D. Zhou, Proceedings of the 2nd International Particle Accelerator Conference (IPAC11), San Sebastian, Spain, 2011, pp. 532-534.
[12] H. Singer, H. Steinbigler, and P. Weiss, IEEE Trans. on Power Apparatus and Systems, Vol. PAS-93, No. 5, pp. 1660-1668, 1974.
[13] N. H. Malik, IEEE Trans. on Electrical Insulation, Vol. 24, No. 1, pp. 3-20, 1989.
[14] A. W. Chao and M. Tigner (eds.), Handbook of Accelerator Physics and Engineering (World Scientific, Singapore, 1999), p. 559.